## PAPER

Check for updates

# β-tricalcium phosphate synthesized in organic medium for controlled release drug delivery application in bio-scaffolds†

Md. Sahadat Hossain, [ID] [a] Md. Aftab Ali Shaikh,*[ac] Md. Najem Uddin, [ID] [b] Muhammad Shahriar Bashar [ID] [d] and Samina Ahmed [ID] *[ab]

β-tricalcium phosphate (β-TCP) was synthesized in an organic medium (acetone) to obtain a single-phase product while calcium carbonate ($CaCO_3$) and *ortho*-phosphoric acid ($H_3PO_4$) were the sources of Ca, and P, respectively. The synthesized β-TCP was characterized by employing a number of sophisticated techniques vis. XRD, FTIR, FESEM, VSM and UV-Vis-NIR spectrometry. On the other hand, cytotoxicity, hemolysis, and antimicrobial activity for Gram-negative as well as Gram-positive (*E. coli* and *S. aureus*) bacteria were explored using this synthesized sample in powder format. However, to assess the drug loading and releasing profile, these powdered samples were first compressed into disks followed by sintering at 900 °C. Prior to loading the drug, porosity, density, and water absorbance characteristics of the scaffolds were examined in deionized water. Both loading and releasing profiles of the antibiotic (ciprofloxacin) were looked over at various selected time intervals which were continued up to 28 days. The observed results revealed that 2.87% of ciprofloxacin was loaded while 37% of this loaded drug was released within the selected time frame as set in this study. The scaffold was also immersed in SBF solution maintaining identical interim periods for the bioactivity evaluation. Furthermore, all three types of samples (*e.g.* drug-loaded, drug-released, and SBF-soaked) were characterized by FESEM and EDX while antimicrobial activity (against *E. coli*, *S. typhi*, and *S. aureus*) and efficacy to prevent hemolysis were also investigated. The drug-loaded scaffold presented a larger inhibition zone than the standard for all three types of microbes. Although powdered β-TCP was inactive in killing the Gram-negative bacteria, surprisingly the drug-released scaffold showed an inhibition zone.

## Introduction

The demand for natural or synthetic biomaterials is increasing day by day for the replacement or regeneration of boney materials associated with trauma, disease, or tumor resection.[1] The market relevant to bone-problem materials has been augmenting and for instance, in 2019 the market value of biomaterials was US$ 3046.7 million which is likely to increase by 5.5% within 2027.[2] The widely used techniques autografts and allografts have a few inherent unavoidable issues such as donor problems, site morbidity, time of rehabilitation, pathogen transmission, development of sepsis, *etc.*[3] which lead to the

[a]*Institute of Glass & Ceramic Research and Testing, Bangladesh Council of Scientific and Industrial Research (BCSIR), Dhaka 1205, Bangladesh. E-mail: shanta_samina@yahoo.com; aftabshaikh@du.ac.bd*

[b]*BCSIR Laboratories Dhaka, Bangladesh Council of Scientific and Industrial Research (BCSIR), Dhaka 1205, Bangladesh*

[c]*Department of Chemistry, University of Dhaka, Dhaka 1000, Bangladesh*

[d]*Institute of Fuel Research & Development, Bangladesh Council of Scientific and Industrial Research (BCSIR), Dhaka 1205, Bangladesh*

† Electronic supplementary information (ESI) available. See DOI: https://doi.org/10.1039/d3ra04904c

search for appropriate biomaterials. Calcium phosphate-based compounds which are widely used as biomaterials in bone defects are hydroxyapatite, α-tricalcium phosphate, β-tricalcium phosphate, tetracalcium phosphate, amorphous calcium phosphate, dicalcium phosphate dihydrate, dicalcium phosphate anhydrous, calcium deficient hydroxyapatite, *etc.*[4] The main component of bone is not tricalcium phosphate but rather hydroxyapatite (HAp) but phosphate ions are deposited on the hydroxyapatite forming a Ca/P ratio of 1.94 which is very similar to tricalcium phosphate.[5] β-Tricalcium phosphate (β-TCP) is well known for its osteoconductivity absorbability, and biocompatibility properties which enable new bone to replace scaffolds.[6–8] In comparison to the HAp, β-TCP is more soluble and degradable in physiological conditions and is favorable for the formation of new bone by replacing scaffolds.[8] Sizes of crystals and the phase purity also contribute to the favorable application of β-TCP as a bio-scaffold. The synthesis processes of β-TCP are precipitation method from $CaCO_3$ and $H_3PO_4$ (ref. 9), solid-state method from dicalcium phosphate and $CaCO_3$ (ref. 10), from calcium deficient hydroxyapatite in methanol solvent,[11] from sodium diphosphate and calcium chloride in ethylene glycol medium,[12] from calcium acetate and phosphoric

acid in methanol solution,[13] *etc.* But, no data were found for the synthesis of β-tricalcium phosphate in acetone medium as well as in-depth biocompatibility analysis along with antibiotic loading and release.

In this research, β-tricalcium phosphate was synthesized in acetone medium and characterized using different instrumental techniques. Scaffolds were prepared in cylinder shape for the ciprofloxacin loading and released up to 28 days and then biocompatibility was assessed engaging cytotoxicity, hemolysis, antimicrobial activity (*S. aureus*, *E. coli* and *S. typhi*) for all the samples.
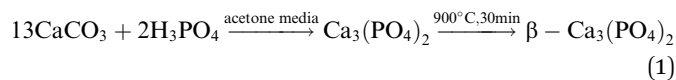
## Materials and methods

### Materials

The analytical grade calcium carbonate, acetone, and *ortho*-phosphoric acid (85% w/w) were procured from E-Merck Germany and no purification process was involved before use. Deionized water (DI) was utilized throughout the process which was prepared through a double distillation process in GRD, IGCRT, BCSIR.

### Methods

**Synthesis of β-tricalcium phosphate.** *Ortho*-phosphoric acid ($H_3PO_4$) and calcium carbonate ($CaCO_3$) were taken as the raw source of phosphate and calcium, respectively. To synthesize β-TCP the molar ratio of the Ca and P was fixed at 1.50, and 5.0 g calcium carbonate was taken along with the required phosphoric acid. The calcium carbonate was taken in a glass bottle and then 100 mL of acetone was added and gently shaken for mixing. After 10 min, *ortho*-phosphoric acid was slowly added from a burette maintaining gentle stirring for uniform mixing. The mixed sample was shaken in an orbital setting 50 rpm, which was kept for 2 h for the completion of interaction. The white precipitate (ppt) was separated out by filtration and then sample was dried in an oven for 2 h. The dried sample was calcined at 900 °C for 30 min maintaining an increment of 3 °C min$^{-1}$ for obtaining crystalline β-$Ca_3(PO_4)_2$.

$$13CaCO_3 + 2H_3PO_4 \xrightarrow{\text{acetone media}} Ca_3(PO_4)_2 \xrightarrow{900°C,30min} \beta - Ca_3(PO_4)_2 \tag{1}$$

The scaffold of the β-TCP powder was formed using 2–3 g of powder sample and pressing the powder at 50 kgf pressure for 5 min. Then, the formed scaffolds were sintered at 900 °C for 5 h.

**Instrumentation.** The phase of the synthesized tricalcium phosphate was explored engaging a Rigaku SE XRD machine which was operated at current and voltage of 40 kV and 50 mA, respectively. The data was recorded from 10 to 70° of 2θ flowing steps of 0.01 and the instrumental temperature was fixed at 19–20° while the mode was Bragg–Brentano parafocusing geometry. The machine was calibrated with the silicon reference standard and the collected data were compared with the standard ICDD database. The functional groups of β-TCP were recognized by employing FTIR instrument (Model: IR-Prestige

21, Shimadzu, Japan) and the instrumental facility was enhanced attaching attenuated total reflectance (ATR) system. The data was recorded within the scanning range of 400–4000 cm$^{-1}$ maintaining an average of 30 scans flowing 4 cm$^{-1}$ spectral resolution. Surface morphology was explored utilizing an FESEM machine (model: JEOL JSM-7610F) and the images was captured maintaining 15 kV accelerating voltage. The optical property of the synthesized material was evaluated by a UV/vis/NIR spectrophotometer of PerkinElmer LAMBDA 1050+ model within the scan range of 250–800 nm wavelength. Solid powdered β-TCP was used as the sample and the operating conditions were 25 °C temperature and 60% relative humidity.

**Hemolysis test.** To assess hemolysis (Hp) character, heparin was chosen as an anti-coagulant agent for collecting fresh blood sample. Physiological saline extract solution and deionized water were taken as the negative and positive control, respectively. Fresh blood sample was taken (0.2 mL) and diluted before incubation at 37 °C for 1 h. Different combinations of the sample such as 50, 100, and 200 μg mL$^{-1}$ were prepared and reserved for 2 h for proper interaction. The sample was centrifuged at 3000 rpm for 5 min before taking absorbance of the supernatant using a UV-spectrophotometer at 545 nm. The Hp percentage was estimated using the eqn (2).[14–16]

$$H_p = \frac{A_s - A_{nc}}{A_{pc} - A_{nc}} \times 100 \tag{2}$$

where, $A_S$, $A_{nc}$ and $A_{pc}$ are the average absorbance at 545 nm wavelength for the sample, the negative control, and the positive control, tandemly.

**Cytotoxicity assessment.** The percentages of viable and non-viable cells were estimated engaging the Trypan Blue Exclusion method where Vero cell (CLS 605372, Germany) of kidney from the African green monkey was taken. Different combinations of the sample such as 50, 100, and 200 μg mL$^{-1}$ were prepared and before interaction with cell, β-TCP was stream sterilized for 1 h. Using an automated cell counter instrument (LUNA-II™, Analytikjena), the viable and non-viable cells were counted after 72 h of 1 mL of suspension, and a similar procedure was described elsewhere.[17,18] The cell viability percentages were computed using the eqn (3).[17,19]

$$\text{Percentage of viable cells} = \frac{\text{Number of viable cells}}{\text{Total number of cells}} \times 100 \tag{3}$$

For the analysis of scaffold, the scaffolds were finely grounded and mixed thoroughly for uniform mixing. Then, powdered samples were taken for cytotoxicity analysis and followed the previously mentioned procedure.

**Antimicrobial activity test.** *Staphylococcus aureus* (*S. aureus*) (ATCC 9144) as Gram-positive bacteria and *Escherichia coli* (*E. coli*) (ATCC 11303) as Gram-negative bacteria were chosen to explore antimicrobial activity engaging agar well diffusion method. 0.5 McFarland standard turbidity and fresh culture were uniformly spread over the agar media. A sterile cork borer was utilized to prepare well with 6 mm diameter, and 50 μL of 200 μg mL$^{-1}$ sample was poured in each well. Kanamycin (30 μg) and DMSO (5%) were chosen as positive and negative

control, respectively which were reserved for 3 h at 4 °C for uniform diffusion. The incubation of the plate was performed at 37 °C for 24 h, and then the diameter of the zone of inhibition was estimated.

**Antibiotic loading and releasing.** To assess drug loading and release profile, ciprofloxacin was chosen as a model drug. The drug loading was performed using 500 ppm of ciprofloxacin solution which was prepared in DI water medium. Round shape scaffolds with variation in diameter of 12.5–13 mm and thickness of 1.5–2.0 mm were prepared using compressing and then sintering at 900 °C. A number of scaffolds were immersed in 20 mL of drug solution and UV-absorbance was counted after different time interval up to 28 days. The drug loaded samples were then immersed in SBF (simulated body fluid) solution for the study of release profile up to 28 days. The detail procedures of drug loading and releasing followed as described in the literature.[20] SBF was prepared following a well-established procedure in brief Briefly, NaCl: 8.0756 g, NaHCO$_3$:0.3532 g, KCl: 0.2250 g, K$_2$HPO$_4$·3H$_2$O: 0.2310 g, MgCl$_2$·6H$_2$O: 0.3033 g, CaCl$_2$·6H$_2$O: 0.3638 g, and Na$_2$SO$_4$: 0.0716 g in addition to this solution pH was maintained using 6.0658 g of tris(hydroxymethyl)aminomethane and 0.1 M HCl solution.[21] Drug loading and release profile were analyzed utilizing the eqn (4) and (5), and the details can be found elsewhere.[22]

$$\text{Drug loading} = \frac{\text{Weight of drug loaded}}{\text{Weight of scafold}} \times 100 \qquad (4)$$

$$\text{Drug release} = \frac{\text{Amount of drug release}}{\text{Amount of drug loaded}} \times 100 \qquad (5)$$

**Statistical analysis.** One-way Analysis of Variance (ANOVA) test was accomplished to compare the data of biomaterials and the value $p < 0.05$ was assumed as statistically significant on the other hand $p > 0.05$ was presumed statistically non-significant.[23] The ANOVA test was implemented using an Origin Pro software and the details are described elsewhere.[18]

# Results and discussion

## Characterization

The phase of synthesized β-TCP was evaluated by utilizing X-ray diffraction (XRD) technique and generated pattern is presented in Fig. 1A. The noticeable diffraction of the generated pattern in terms of $d$-spacing and crystal planes were matched with the standard ICDD database (card no#: 04-006-9376). No other phase was found in the pattern except rhombohedral β-TCP of $R3c$ space group[24] and a similar type of β-TCP has been reported in the literature.[20,25] Rietveld refinement was done to quantify the phase percentage of β-TCP and hydroxyapatite (HA, card no#:01-074-0566) by using Rigaku Smart Lab Studio II software. The search and matching technique of the Rietveld refinement [$R_{wp}$ = 15.58%, $R_p$ = 11.44, $S$ = 0.97] revealed that the synthesized product contained 95.8% β-TCP ($a$ = 10.33 Å, $b$ = 10.33 Å, $c$ = 37.13 Å, lattice volume = 3436 Å$^3$) and 4.2% HA ($a$ = 9.41 Å, $b$ = 9.41 Å, $c$ = 7.00 Å, lattice volume = 537 Å$^3$). Only 4 (2$\theta$ = 25.85, 31.90, 41.87, and 48.26°) very small peaks (relative intensity

∼1%) out of total 46 peaks were not coincided with the mentioned standard. Few peaks were similar both for the β-TCP and HAp thus the percentages of HAp were higher. Calculated crystallite size of the synthesized product was 70 nm from the Scherrer equation. Fig. 1B represents the FTIR image of β-TCP which generate transmittance peaks for the occurrence of the phosphate group. The stretching vibrations ($\nu_1$) of PO$_4^{3-}$ group were recorded at 948, and 972 cm$^{-1}$ wavenumber whereas bending vibration ($\nu_2$) appeared at 458 cm$^{-1}$ wavenumber. A very strong peak originated at 1025 cm$^{-1}$ due to P–O stretching of triply degenerate ($\nu_3$) vibration and bending of triply degenerate ($\nu_4$) of P–O generated peaks at 551 and 600 cm$^{-1}$ wavenumber. A similar type of FTIR spectrum has been reported in the literature.[26] FESEM image of the synthesized product is revealed in Fig. 1C. Although the particles mostly remained in cluster form but a variation in size and shape was clearly evident. As the powder sample was chosen for the image capture, there remained vacant space inside the particles. These types of gradient grain size image of β-TCP were reported in the literature.[27] Magnetic property of the synthesize β-TCP is revealed in Fig. 1D which is measured engaging a vibrating sample magnetometer (VSM) at room temperature. Magnetic field and magnetic nanoparticles are drawing researchers' attention for the targeted drug delivery, tissue repair and cancer therapy,[28] but no feromagnetic property was visualized for the sample. Very low magnetization (0.3 emu/g) was noticed for the synthesized β-TCP in acetone media. No significant hysteresis was also noticed for the applied magnetic field and a similar type of paramagnetic behavior of the β-TCP was also reported.[29,30] Fig. 1E represents the diffuse reflection spectra (DRS) spectra of β-TCP. With the aid of Kubelka–Munk function, details are explained elsewhere,[31] the optical band gap energy (3.88 eV) was calculated which is visualized here in Fig. 1F.

## *In vitro* assessment as bio-materials

The fruitful applications such as electrochemical biosensors, bioimaging, drug delivery, bone implants fabrication, *etc.*,[32,33] of any biomaterials are primarily depended on the data of cytotoxicity evaluation. In the case of β-TCP, the cytotoxicity performance was explored at various sample concentration such as 50, 100 and 200 μg mL$^{-1}$, and the pictorial views are represented in Fig. 2A–C, respectively. Automatic counted cell viable percentages are pictured in Fig. 2D which shows good viable percentage. With the increment of sample dose form 50 μg mL$^{-1}$ to 200 μg mL$^{-1}$, the percentages of viable cells were decreased from 98% to 96%. The control sample was also prepared using dimethyl sulfoxide (DMSO) and the viable percentage was ∼98%. The ISO-10993 guideline (which emphasized that for any biomaterials to be considered as non-cytotoxic and biocompatible[34]) must exhibit cell viability more than 70% was followed in case of cytotoxicity test evaluation. The data of the cytotoxicity analysis showed good correlation ($R^2$ = 0.9925, $p$ < 0.03887). The cell viability percentages of synthesized β-TCP in acetone medium can be comparable to the other reported viable percentage of biomaterials such as 84% for gellan gum,[35] more than 96% for fish scale collagen
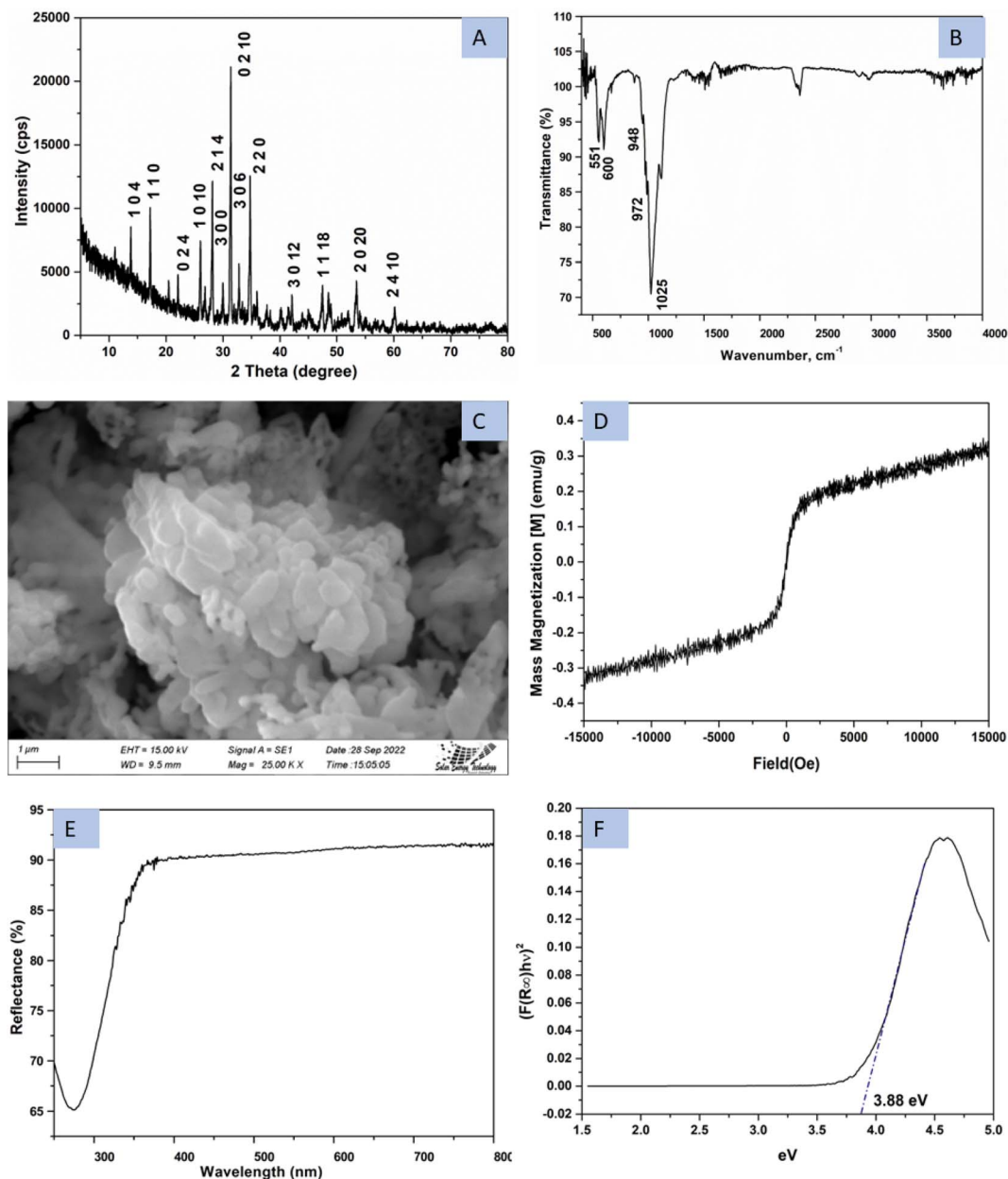
Fig. 1 Characterization of synthesized TCP using (A) XRD, (B) FTIR, (C) FESEM, (D) VSM, (E) UV-vis-NIR spectrum, and (F) optical bandgap energy.

membrane,[36] 85% for Zn–Mg composites,[37] 83–99% for composites of β-TCP, *etc.*

Hemolysis performance was explored from the ability of breakdown of RBC (Red Blood Cell) at various sample doses and the calculated data are visualized in Fig. 2E. When the sample quantity was lower, the hemolysis percentage was 2.4% which remained in the highly hemo-compatible region. With the increment of β-TCP quantity the evaluation of material changed from highly hemo-compatible to hemo-compatible region.[17] There are many factors such as size of particles, nanoparticle shape, surface modification, surface charge, and roughness are responsible for the hemolysis.[38] As the β-TCP remained in the hemo-compatible region, no further evaluation was executed.

The *S. aureus* (Fig. 2F) and *E. coli* (Fig. 2G) bacteria were chosen as the model to evaluate the antimicrobial performance of the synthesized sample as maximum bone infections are responsible for these two bacteria.[39] Inhibition zone was found in the case of *S. aureus* (Gram positive) bacteria but no effect was visualized for *E. coli* (Gram negative) bacteria. The diameter of inhibition zone for standard was 18 mm in the case of *E. coli* whereas 20 and 30 mm for standard and TCP sample, respectively, in the case of *S. aureus*. There is a variation in the cell wall of Gram positive (<10 nm) and Gram negative (20–80 nm) which may influence the formation of inhibition zone in the case of Gram positive bacteria.[40] The structure of the two types of bacteria is different such as the bilayer of Gram negative bacteria consists of inner and outer membrane and the
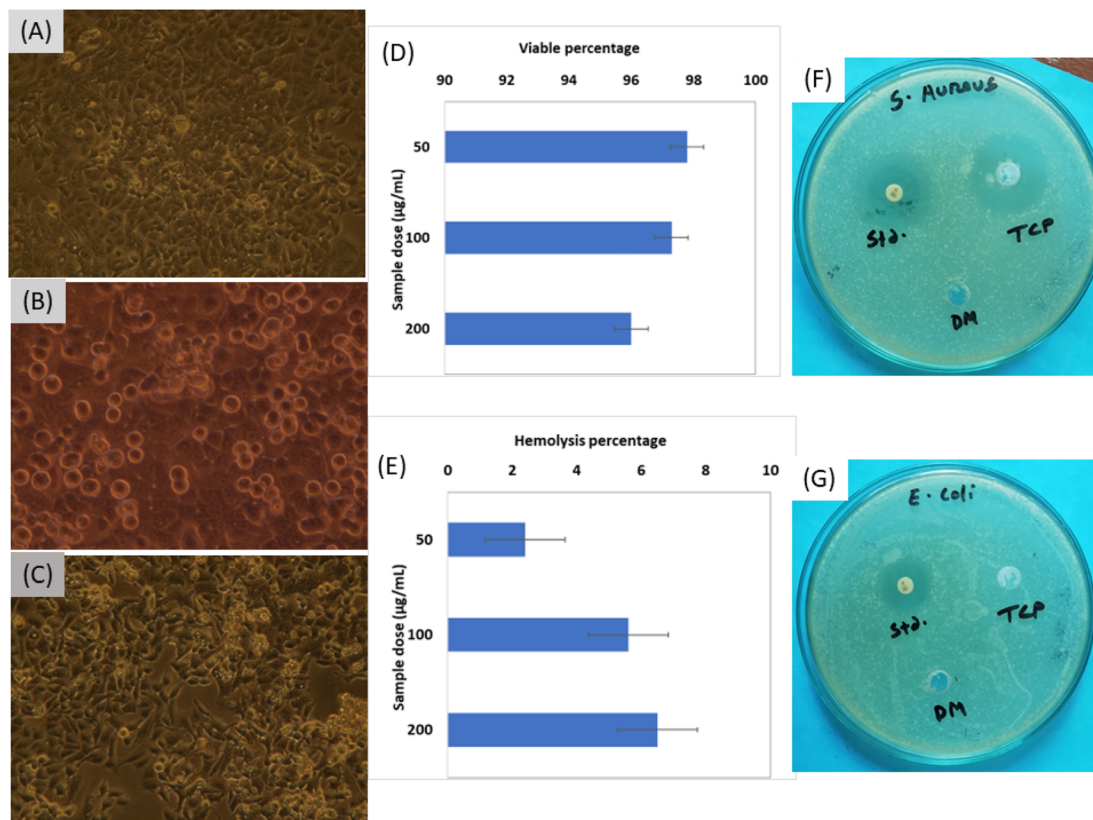
**Fig. 2** Evaluation of (A) cell viable image at 50 µg mL$^{-1}$, (B) cell viable image at 100 µg mL$^{-1}$, (C) cell viable image at 200 µg mL$^{-1}$, (D) cell viability percentage, (E) hemolysis percentage, (F) antimicrobial activity on *S. aureus*, (G) antimicrobial activity on *E. coli*.
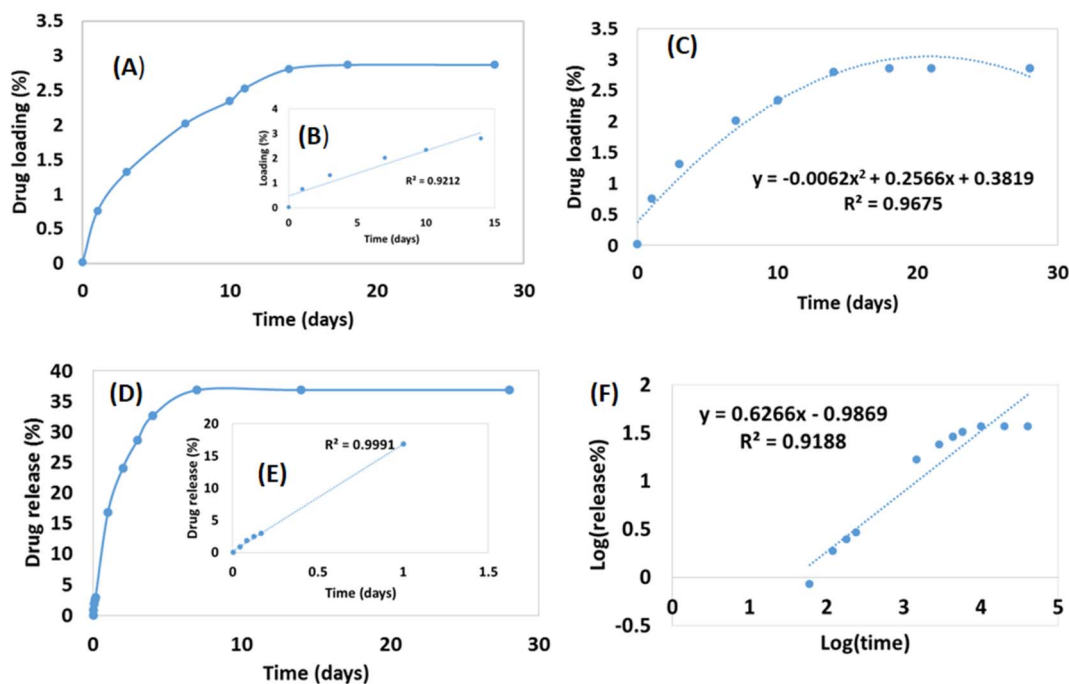


**Fig. 3** Drug loading and release profile for (A) 28 days loading, (B) 14 days loading, (C) 28 days loading using binomial equation, (D) release at 28 days, (E) release for 24 h, and (F) release using Korsmeyer–Peppas model for 28 days.

periplasm inner space between [41] while in the case of component of cell wall of Gram positive bacteria are teichoic acids or similar polysaccharides, glycopolymer and proteins.[42] The complex cell wall of Gram-negative *E. coli* is harder to break-down than the Gram-positive bacteria thus inhibition zone was form for Gram positive bacteria.

## Characterization of scaffold

The scaffold was prepared using no binding agent and in the tablet shape with an average diameter of 13.0 mm and 1.0 mm thickness. The porosity of the prepared scaffold was estimated from $p = (M_2 - M_1)/\rho V$ formula[39] where $M_2$, $M_1$, $\rho$, and $V$ are the final weight after 5 min soaking in DI water, initial weight of the scaffold, density of water and volume of the scaffold, respectively. The calculated porosity percentage was 52.3% ($\pm 3$). The water absorbance percentage was computed from the ratio of water gain to the weight of scaffold at room temperature and the value was 22% ($\pm 2$). Free moisture content was 0.5% ($\pm 0.05$) which was found following the reported methodology at 50 °C temperature.[43] When water was absorbed the volume of the scaffold changed form 133.38 to 136.64 mm$^3$ and the surface area was enhanced from 308.52 to 309.77 mm$^2$. Although 22% water was absorbed by the scaffold, only 2.4% volume was changed. The calculated density was 1.83 g cm$^{-2}$ which was 60% of the theoretical density (3.07 g cm$^{-2}$).[44] Nearly 1.5% weight was gained during the immersion in SBF for 28 days which was found for 50 mL SBF solution.

## Antibiotic loading and releasing profile

Drug loading and release were performed up to 28 days which is visualized in Fig. 3. No material was added to enhance the porosity of the scaffold thus a limited percentage of pore remained inside the scaffold. Thus a lower percentage of drug loading was experienced up to 28 days although within 14 days the loading capacity reached in its peak (2.87%) (Fig. 3A). The literatures also supported this types of drug loading such as 4.4% norfloxacin by hydroxyapatite,[45] 0.19% gentamicin by hydroxyapatite,[46] *etc.* The drug loading up to 14 days increased linearly (inscribed Fig. 3B) with $R^2 = 0.92$, but with the addition of more days the loading remained relatively constant. The loading profile of the drug can be more explained by a binomial equation (Fig. 3C) where the regression coefficient was relatively good ($R^2 = 0.967$). The regression coefficient of the normal straight line for 28 days was comparatively low ($R^2 = 0.70$) thus it can be said that the drug loading followed the polynomial relation in the order of two. If the order of polynomial can be increased, the more accurate regression coefficient can be found like in the order of three of polynomial the regression coefficient was $R^2 = 0.99$. The drug loading for a long time (in this case 28 days) cannot be explained in a liner way it is better to choose a polynomial equation either in the order of two or three.

Drug release profile was performed after the drug loading within 28 days and the scaffold released 36.86% loaded drug (Fig. 3D) which was also evaluated for 28 days. Within 7 days, the drug released reached in its maximum point and then remained constant. Initial high dose of antibiotic is required for the application of scaffold in body as initial attracts of microbes are higher when implant is attached.[46] In this study, an initial high release was recorded such as within 24 h nearly 17% drug was released which maintained a linearity (inscribed Fig. 3E) with $R^2 = 0.99$. However, if the release for 28 days are counted then the linear regression coefficient became very low ($R^2 = 0.46$) and for first 7 days $R^2 = 0.84$. When binomial equation was chosen no significant change was visualized ($R^2 = 0.81$) for 28 days to accept as a good fit. To study the release profile for ciprofloxacin, different model equations were employed such as zero order, first order, Higuchi model, and Korsmeyer-Peppas Model. The zero order and first order kinetics exerted low regression coefficient ($R^2 = 0.46$ for zero order and 0.49 for first order) for 28 days and details of procedures are reported else-where.[47] The Higuchi kinetic release models also revealed lower regression coefficient ($R^2 = 0.75$). On the other hand, the Korsmeyer–Peppas model[48] presented relatively better fit for the drug release up to 28 days ($R^2 = 0.92$) (Fig. 3F). From the slope value (0.63), it can be predicted that the diffusion transport followed non-Fickian diffusion mechanism.

## *In vitro* assessment after antibiotic loading and releasing

Fig. 4 represents the SEM, EDX and antimicrobial images of the prepared scaffolds and the scaffold was chosen as after drug loading up to 28 days (denoted as *L*), drug releasing up to 28 days (denoted as *R*) and soaking in SBF solution up to 28 days (denoted as *S*). Very small amount of drug was loaded in the porous scaffold and different types of particles were visualized the SEM images (Fig. 4A and B). There was no regular porosity as the necking was occurred randomly which was in tune with the drug loading behavior of binomial-equation model. Drug molecules captured the surface of pore and after certain percentage more drugs were unable to enter the pore which made the constant loading after few days and followed binomial equation. There was no significant variation in the elemental analysis from EDX (shown in (ESI) Fig. S1†) which carried good evidence of drug loading in the bulk of scaffold not only on the surface. When drug was released on the SBF solution for 28 days no significant change was noticed in the scaffold (sample *R*) (Fig. 4D and E) neither in the particle shape nor on the porosity along with elemental analysis (ESI Fig. S2†). A very similar phenomenon was visualized when normal scaffold (sample S) was immersed in the SBF solution for 28 days (Fig. 4G and H). There was a 0.8% ($\pm 0.12$) weight gain when scaffold was immersed in SBF solution which was measured after 105 °C for 4 h drying condition. Instead of gaining 0.8% metal or metal salt no significant change was recorded in the elemental analysis (ESI Fig. S3†) this may be the bulk accumulation instead of surface.

Antimicrobial activity of the Gram-positive and Gram-negative bacteria was evaluated for the drug loaded (*L*), drug released (*R*), scaffold in SBF (*S*), standard (std) and DMSO (*D*) sample which are presented in Fig. 4C, F and I. All the three bacteria *S. aureus*, *E. coli* and *S. typhi* (ATCC-13311) revealed antimicrobial properties even for the scaffold of drug released
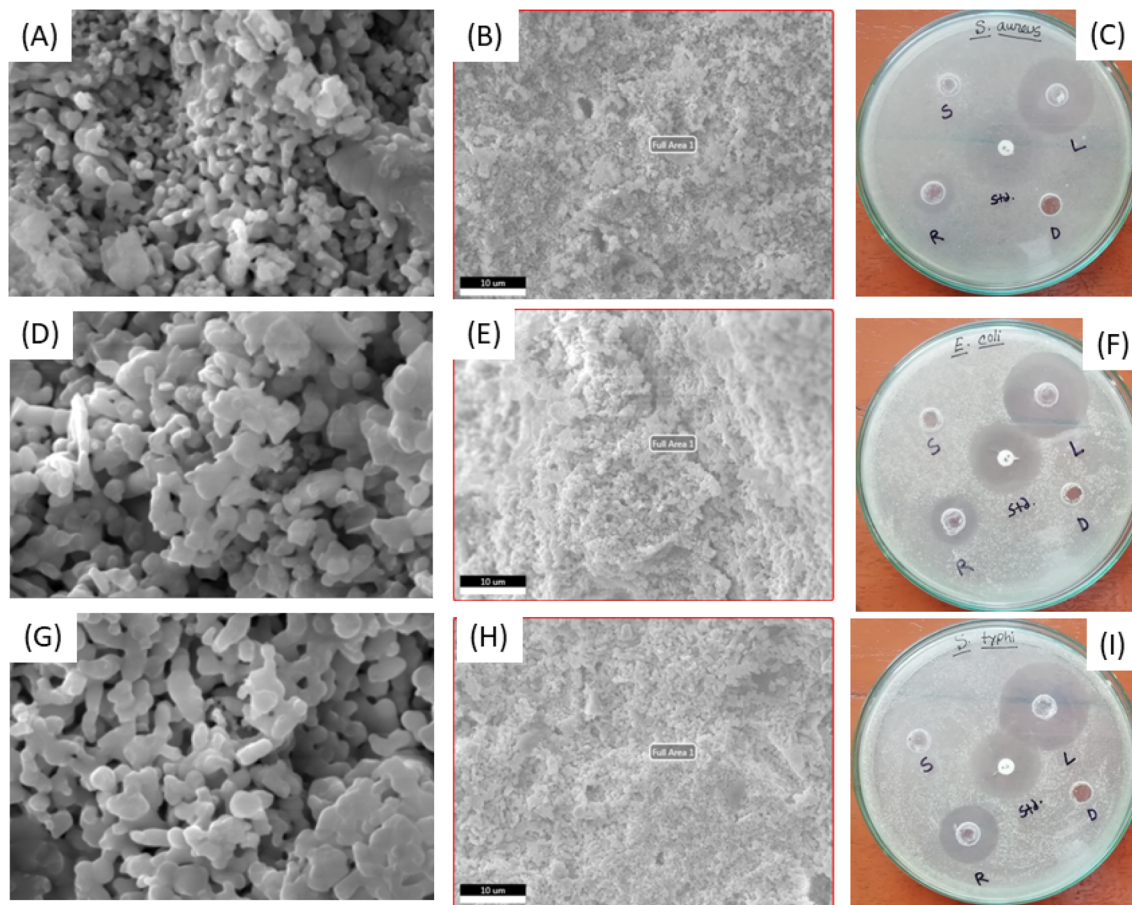
**Fig. 4** Pictorial view of drug loaded sample (A) SEM image, (B) selected are for EDX, (C) antimicrobial effect on S. aureus, (D) SEM image after drug release, (E) area for EDX of drug release, (F) antimicrobial effect on *E. coli*, (G) SEM of SBF sample, (H) area for SBF sample, and (I) antimicrobial activity on *S. typhi*.

**Table 1** Hemolysis percentage of drug loaded sample within 28 days, drug released sample in 28 days and soaked sample in SBF up to 28 days

| Sample conc. ($\mu g\ ml^{-1}$) | Drug loaded | Drug released | In SBF solution |
|---|---|---|---|
| 50 | 1.4 | 1.2 | 0.8 |
| 100 | 2.8 | 1.8 | 2.2 |
| 200 | 4.2 | 2.6 | 3.8 |

up to 28 days however scaffold in SBF (and DMSO) failed to show any antimicrobial activity. The diameters (in mm) of the inhibition zone followed a regular pattern for *S. aureus* ($L = 34$, Std = 24, $R = 16$), *E. coli* ($L = 36$, Std = 30, $R = 18$) and *S. typhi* ($L = 38$, Std = 28, $R = 24$). The drug loaded sample showed larger inhibition zone than the standard and the drug released (up to 28 days) sample also exerted inhibition zone. Normal powder sample failed to kill the Gram-negative bacteria (*E. coli*) which is presented in the previous section but drug loaded or released scaffold killed the Gram-negative bacteria. To justify the killing property of Gram-negative bacteria another Gram negative (*S. typhi*) bacterial was experimented and found similar characteristic. Relatively good inhibition zone was found in the case of

drug loaded and released scaffold than few reported articles.[39,49] Highly hemocompatibility was observed for the presence of drug and salt/metal ions from SBF solution which is recorded in Table 1. Though the RBC break down was increased with the enhancement of sample doses, all of values remained in the highly hemo-compatible region as described in the literature.[17,18]

## Conclusion

Inorganic biomaterial (β-tricalcium phosphate) can be synthesized in acetone media for more pure phase from calcium carbonate and phosphoric acid through facile synthesis route. High released profile was recorded in the first 24 h which is very crucial for combating initial attract of microbes during implant surgery in body. Pure β-TCP cannot kill Gram-negative (*E. coli*) bacteria but when ciprofloxacin was loaded (even after release of antibiotic for up to 28 days) scaffold can kill *E. coli* along with *S. typhi*. Ciprofloxacin loading followed bionomial equation and release profile followed Korsmeyer–Peppas model when data were recorded for 28 days. Highly hemocompatible property was also found for the scaffold in experimental conditions. It is suggested from this research that β-tricalcium phosphate can

be synthesized in acetone medium for the successful application as scaffold with ciprofloxacin loading as *in situ* application of antibiotic.

## Data availability

Data will be made available on request.

## Author contributions

Md. Sahadat Hossain conceived and designed the experiment, analysed the data, written the original manuscript and performed the experiment. Md. Aftab Ali Shaikh supervised the overall work, assisted in writing the manuscript and managed the required facilities. Md. Najem Uddin executed the cytotoxicity, hemolysis and antimicrobial properties. Muhammad Shahriar Bashar executed FESEM and EDX analysis. Samina Ahmed supervised the overall work, managed the required facilities and assisted in writing the manuscript.

## Conflicts of interest

There are no conflicts to declare.

## Acknowledgements

## References

1 L. Vidal, C. Kampleitner, M. Á. Brennan, A. Hoornaert and P. Layrolle, Reconstruction of large skeletal defects: current clinical therapeutic strategies and future directions using 3D printing, *Front. bioeng. biotechnol.*, 2020, **8**, 61.

2 I. Coherent, Bone Graft And Substitutes Market Size And Forecast To 2027, n.d., https://www.coherentmarketinsights.com/market-insight/bone-graft-and-substitutes-market-1050?&campaignid=19256539599&keyword=bone%20defects&gclid=CjwKCAiAhqCdBhB0EiwAH8M_GtmeLeh5_88Bp4ilQ3dudCkgxLI8hvVdWnbKYAsSVh7CMwolWsxZJRoCGXsQAvD_BwE, accessed December 26, 2022.

3 J. Banerjee, E. Radvar and H. S. Azevedo, Self-assembling peptides and their application in tissue engineering and regenerative medicine, in *Peptides and Proteins as Biomaterials for Tissue Regeneration and Repair*, Elsevier, 2018, pp. 245–281.

4 I. Lodoso-Torrecilla, R. K. Gunnewiek, E.-C. Grosfeld, R. B. de Vries, P. Habibović, J. A. Jansen and J. J. van den Beucken, Bioinorganic supplementation of calcium phosphate-based bone substitutes to improve *in vivo* performance: a systematic review and meta-analysis of animal studies, *Biomater. Sci.*, 2020, **8**, 4792–4809.

5 J. Govaerts, Isotopic exchanges and the existence of tricalcium phosphate in bone, *Nature*, 1954, **174**, 831–832.

6 N. Kikuchi, T. Yoshioka, N. Arai, K. Hyodo, A. Kanamori and M. Yamazaki, A radiological study of bone remodeling with two different types of porous β-tricalcium phosphate in humans, *Sci. Rep.*, 2020, **10**, 1–7.

7 V. H. Arkin, U. Narendrakumar, H. Madhyastha and I. Manjubala, Characterization and *in vitro* evaluations of injectable calcium phosphate cement doped with magnesium and strontium, *ACS Omega*, 2021, **6**, 2477–2486.

8 W. Huang, Y. Yang, Z. Mao, J. Li and Q. Wu, Sacrificed Carbon-Assisted Synthesis of β-Tricalcium Phosphate Nanostructures, *Cryst. Growth Des.*, 2016, **16**, 5159–5165.

9 H. Chaair, H. Labjar and O. Britel, Synthesis of β-tricalcium phosphate, *Morphologie*, 2017, **101**, 120–124.

10 R. Famery, N. Richard and P. Boch, Preparation of α-and β-tricalcium phosphate ceramics, with and without magnesium addition, *Ceram. Int.*, 1994, **20**, 327–336.

11 J.-S. Bow, S.-C. Liou and S.-Y. Chen, Structural characterization of room-temperature synthesized nano-sized β-tricalcium phosphate, *Biomaterials*, 2004, **25**, 3155–3161.

12 L. Galea, M. Bohner, J. Thuering, N. Doebelin, C. G. Aneziris and T. Graule, Control of the size, shape and composition of highly uniform, non-agglomerated, sub-micrometer β-tricalcium phosphate and dicalcium phosphate platelets, *Biomaterials*, 2013, **34**, 6388–6401.

13 C. Makarov, I. Gotman, X. Jiang, S. Fuchs, C. J. Kirkpatrick and E. Y. Gutmanas, In situ synthesis of calcium phosphate-polycaprolactone nanocomposites with high ceramic volume fractions, *J. Mater. Sci.: Mater. Med.*, 2010, **21**, 1771–1779.

14 S. Singh, M. M. Alrobaian, N. Molugulu, N. Agrawal, A. Numan and P. Kesharwani, Pyramid-shaped PEG-PCL-PEG polymeric-based model systems for site-specific drug delivery of vancomycin with enhance antibacterial efficacy, *ACS Omega*, 2020, **5**, 11935–11945.

15 A. I. Foudah, M. H. Alqarni, S. A. Ross, A. Alam, M. A. Salkini and P. Kumar, Site-Specific Evaluation of Bioactive Coumarin-Loaded Dendrimer G4 Nanoparticles against Methicillin Resistant Staphylococcus aureus, *ACS Omega*, 2022, **7**, 34990–34996.

16 M. E. Fait, M. Hermet, F. Comelles, P. Clapés, H. A. Alvarez, E. Prieto, V. Herlax, S. R. Morcelle and L. Bakás, Microvesicle release and micellar attack as the alternative mechanisms involved in the red-blood-cell-membrane solubilization induced by arginine-based surfactants, *RSC Adv.*, 2017, **7**, 37549–37558.

17 S. Sultana, M. S. Hossain, M. Mahmud, M. B. Mobarak, M. H. Kabir, N. Sharmin and S. Ahmed, UV-assisted synthesis of hydroxyapatite from eggshells at ambient temperature: cytotoxicity, drug delivery and bioactivity, *RSC Adv.*, 2021, **11**, 3686–3694.

18 Md. S. Hossain, Md. N. Uddin, S. Sarkar and S. Ahmed, Crystallographic dependency of waste cow bone, hydroxyapatite, and β-tricalcium phosphate for biomedical application, *J. Saudi Chem. Soc.*, 2022, **26**, 101559, DOI: **10.1016/j.jscs.2022.101559**.

19 S. Ponnusamy, R. Subramani, S. Elangomannan, K. Louis, M. Periasamy and G. Dhanaraj, Novel Strategy for Gallium-Substituted Hydroxyapatite/Pergularia daemia Fiber Extract/Poly (N-vinylcarbazole) Biocomposite Coating on Titanium for Biomedical Applications, *ACS Omega*, 2021, **6**, 22537–22550.

20 C. Ching Lau, P. J. T. Reardon, J. Campbell Knowles and J. Tang, Phase-tunable calcium phosphate biomaterials synthesis and application in protein delivery, *ACS Biomater. Sci. Eng.*, 2015, **1**, 947–954.

21 L. Gritsch, M. Maqbool, V. Mouriño, F. E. Ciraldo, M. Cresswell, P. R. Jackson, C. Lovell and A. R. Boccaccini, Chitosan/hydroxyapatite composite bone tissue engineering scaffolds with dual and decoupled therapeutic ion delivery: copper and strontium, *J. Mater. Chem. B*, 2019, 7, 6109–6124, DOI: **10.1039/C9TB00897G**.

22 M. Zhang, Y. Liao, X. Tong and F. Yan, Novel urea derivative-loaded PLGA nanoparticles to inhibit caries-associated Streptococcus mutans, *RSC Adv.*, 2022, **12**, 4072–4080.

23 K. Mishima, Y. T. Okabe, M. Mizuno, K. Ohno, H. Kitoh and S. Imagama, Efficacy of soluble lansoprazole-impregnated beta-tricalcium phosphate for bone regeneration, *Sci. Rep.*, 2022, **12**, 1–10.

24 O. Gokcekaya, K. Ueda, T. Narushima and T. Nakano, Using HAADF-STEM for atomic-scale evaluation of incorporation of antibacterial Ag atoms in a β-tricalcium phosphate structure, *Nanoscale*, 2020, **12**, 16596–16604.

25 J. V. Rau, I. V. Fadeeva, A. S. Fomin, K. Barbaro, E. Galvano, A. P. Ryzhov, F. Murzakhanov, M. Gafurov, S. Orlinskii and I. Antoniac, Sic Parvis Magna: Manganese-substituted tricalcium phosphate and its biophysical properties, *ACS Biomater. Sci. Eng.*, 2019, **5**, 6632–6644.

26 R. G. Carrodeguas and S. De Aza, α-Tricalcium phosphate: Synthesis, properties and biomedical applications, *Acta Biomater.*, 2011, **7**, 3536–3546.

27 R. Duan, D. Barbieri, F. De Groot, J. D. De Bruijn and H. Yuan, Modulating bone regeneration in rabbit condyle defects with three surface-structured tricalcium phosphate ceramics, *ACS Biomater. Sci. Eng.*, 2018, **4**, 3347–3355.

28 S. Basu and B. Basu, Unravelling doped biphasic calcium phosphate: synthesis to application, *ACS Appl. Bio Mater.*, 2019, **2**, 5263–5297.

29 B. Srinivasan, E. Kolanthai, N. Eluppai Asthagiri Kumaraswamy, R. R. Jayapalan, D. S. Vavilapalli, L. H. Catalani, G. S. Ningombam, N. S. Khundrakpam, N. R. Singh and S. N. Kalkura, Thermally modified iron-inserted calcium phosphate for magnetic hyperthermia in an acceptable alternating magnetic field, *J. Phys. Chem. B*, 2019, **123**, 5506–5513.

30 T. Ates, S. V. Dorozhkin, O. Kaygili, M. Kom, I. Ercan, N. Bulut, F. Firdolas, S. Keser, N. C. Gursoy and I. H. Ozercan, The effects of Mn and/or Ni dopants on the in vitro/in vivo performance, structural and magnetic properties of β-tricalcium phosphate bioceramics, *Ceram. Int.*, 2019, **45**, 22752–22758.

31 C. M. Chingo Aimacana, D. A. Quinchiguango Perez, S. Rocha Pinto, A. Debut, M. F. Attia, R. Santos-Oliveira, D. C. Whitehead, T. Terencio, F. Alexis and S. A. Dahoumane, Polytetrafluoroethylene-like Nanoparticles as a Promising Contrast Agent for Dual Modal Ultrasound and X-ray Bioimaging, *ACS Biomater. Sci. Eng.*, 2021, **7**, 1181–1191.

32 L. Liang, Z. Kong, Z. Kang, H. Wang, L. Zhang and J.-W. Shen, Theoretical evaluation on potential cytotoxicity of graphene quantum dots, *ACS Biomater. Sci. Eng.*, 2016, **2**, 1983–1991.

33 D. Szyba, R. Kubina, K. Młynarek-Żak, A. Radoń, A. Kania and R. Babilas, Evaluation of the biocompability and corrosion activity of resorbable CaMgZnYbBAu alloys, *Sci. Rep.*, 2022, **12**, 21007, DOI: **10.1038/s41598-022-25069-6**.

34 B. T. Vu, V. M. Hua, T.-N. Tang, N. N.-T. Dang, H. T.-T. Cao, T. B. Phan, H. T.-K. Ta, V. H. Pham, Q. N. Tran and T. D. Le, Fabrication of *in situ* crosslinking hydrogels based on oxidized alginate/N, O-carboxymethyl chitosan/β-tricalcium phosphate for bone regeneration, *J. Sci.: Adv. Mater. Devices*, 2022, **7**, 100503.

35 M. Matsusaki, H. Ikeguchi, C. Kubo, H. Sato, Y. Kuramochi and D. Takagi, Fabrication of perfusable pseudo blood vessels by controlling sol–gel transition of gellan gum templates, *ACS Biomater. Sci. Eng.*, 2019, **5**, 5637–5643.

36 K.-Y. Li, H.-A. Pan, K.-H. Chen, T.-L. Kuo, C.-H. Chou, Y.-J. Liang and F.-H. Lin, Fish-scale collagen membrane seeded with corneal endothelial cells as alternative graft for endothelial keratoplasty transplantation, *ACS Biomater. Sci. Eng.*, 2019, **6**, 2570–2577.

37 H. Yang, X. Qu, W. Lin, D. Chen, D. Zhu, K. Dai and Y. Zheng, Enhanced osseointegration of Zn-Mg composites by tuning the release of Zn ions with sacrificial Mg-rich anode design, *ACS Biomater. Sci. Eng.*, 2018, **5**, 453–467.

38 S. Mukhopadhyay, H. Veroniaina, T. Chimombe, L. Han, W. Zhenghong and Q. Xiaole, Synthesis and compatibility evaluation of versatile mesoporous silica nanoparticles with red blood cells: an overview, *RSC Adv.*, 2019, **9**, 35566–35578.

39 W. He, Z. Wu, Z. Wu, Y. Cai, Z. Cui, B. Yu and Y. Hong, Construction of Antimicrobial Material-Loaded Porous Tricalcium Phosphate Beads for Treatment of Bone Infections, *ACS Appl. Bio Mater.*, 2021, **4**, 6280–6293.

40 A. Mai-Prochnow, M. Clauson, J. Hong and A. B. Murphy, Gram positive and Gram negative bacteria differ in their sensitivity to cold plasma, *Sci. Rep.*, 2016, **6**, 1–11.

41 S. I. Miller and N. R. Salama, The gram-negative bacterial periplasm: Size matters, *PLoS Biol.*, 2018, **16**, e2004935.

42 L. G. Harris, Microbial Cell Structure and Organization: Bacteria, *Encyclopedia of Infection and Immunity*, 2022, 345–362.

43 M. S. Hossain, M. A. A. Shaikh and S. Ahmed, Synthesis of Gypsum fertilizer from waste eggshells for sustainable environment, *Mater. Adv.*, 2023, **4**, 240–247.

44 B. Dickens, L. W. Schroeder and W. E. Brown, Crystallographic studies of the role of Mg as a stabilizing impurity in β-Ca₃(PO₄)₂. The crystal structure of pure β-Ca₃(PO₄)₂, *J. Solid State Chem.*, 1974, **10**, 232–248.

45 B. J. Melde and A. Stein, Periodic macroporous hydroxyapatite-containing calcium phosphates, *Chem. Mater.*, 2002, **14**, 3326–3331.

46 K. Rajesh, M. K. Rangaswamy, C. Zhang, S. Haldar, M. Kumarasamy, A. Agarwal, P. Roy and D. Lahiri, Surface modified metallic orthopedic implant for sustained drug release and osteocompatibility, *ACS Appl. Bio Mater.*, 2019, **2**, 4181–4192.

47 S. Dash, P. N. Murthy, L. Nath and P. Chowdhury, Kinetic modeling on drug release from controlled drug delivery systems, *Acta Pol. Pharm.*, 2010, **67**, 217–223.

48 S. M. Sreedharan and R. Singh, Ciprofloxacin functionalized biogenic gold nanoflowers as nanoantibiotics against pathogenic bacterial strains, *Int. J. Nanomed.*, 2019, **14**, 9905.

49 A. Nigam and S. J. Pawar, Structural, optical, antimicrobial properties with drug loading and drug release of five different ZnO nano and sub-micron particles for biomedical applications, *Mater. Technol.*, 2021, 1–9.